Journal of Alloys and Compounds 831 (2020) 154701

Contents lists available at ScienceDirect

Journal of Alloys and Compounds

journal homepage: http://www.elsevier.com/locate/jalcom

Quasi-gradient variation of microstructures and properties of Cu–Sn alloy along the thickness direction under cold spinning

Jun Hui , Wenguan Liu **, Biao Wang *

Sino-French Institute of Nuclear Engineering and Technology, Sun Yat-Sen University, Zhuhai, 519082, China

A R T I C L E I N F O

Article history:
Received 30 November 2019
Received in revised form
6 March 2020
Accepted 8 March 2020
Available online 17 March 2020

Keywords:
Quasi-gradient variation
Cu–Sn alloy
Spinning
EBSD
Mechanical properties

A B S T R A C T

During cold spinning, the grain size, grain boundary angle and tensile strength of Cu– Sn alloy show quasi gradient changes in the thickness direction (TD) of hollow cylinder. According to a mechanical analysis, electron backscattering diffraction observations (EBSD), and a finite element simulation, the grain size of Cu–Sn alloy after spinning increases from the outer surface to the inner surface. The number of ultrafine grains was largest on the outer surface, and the original grain boundaries were retained on the inner surface. All of the grain orientations from the outer surface to the inner surface were randomly distributed. An analysis of the grain misorientation suggested that low-angle grain boundaries (LAGBs; <10°), most of which were distributed in the large grain region, accounted for the largest proportion of grains along the TD. The proportion of high-angle grain boundaries (HAGBs; >10°) was inversely proportional to that of LAGBs, the grain boundary energy (GBE) of the HAGBs decreased with increasing number of LAGBs, and the number of HAGBs also decreased gradually. According to tensile tests at room temperature, the outer surface exhibited the highest ultimate tensile strength and the inner surface exhibited the greatest plasticity.

1. Introduction

Spinning is a representative metal forming process in which processes such as forging and extrusion are integrated [1–4]. In spinning, friction is applied to a billet as a spinning wheel is rotated [5,6]. The relationship between the position on the billet at which friction is applied and the relative position of the spinning wheel changes constantly during the rotation of each material point on the billet [7–9]. As a result, the deformation flow of metal along the radial direction of the billet is clearly uneven, causing the material to exhibit discontinuous plastic deformation on the surface and along the thickness direction (TD). Researchers have developed a completely theoretical model of the plastic deformation mechanism of a billet surface during spinning. Xu et al. [10–14] used an elastic–plastic finite element method and microstructural characterization to summarize the mechanism of hot spinning and the relationship between the strength and toughness of a titanium alloy. A three-dimensional finite element analysis mechanical model has been established, and the stress distribution and joint force distribution in different stages of spinning have been extracted; in addition, the effects of the spinning wheel attack angle, feed ratio, and thinning rate on the spinning pressure during spinning deformation have been analyzed, and the nature of the microstructural changes during hot spinning has been determined [15–20]. Zhan et al. [21,22] suggested that the spinning behaviour of light alloys reflects mainly thermal deformation. However, little research has been conducted on cold plastic deformation along the TD, for two main reasons: (1) the material thinning rate is significantly increased during hot spinning, and almost no tissue changes occur along the TD during this process; and (2) under cold deformation by spinning, the thinning rate of the material is limited, and quasi-gradient variation of the microstructure may occur along the TD. This variation results in unstable mechanical properties along the TD, which can easily cause material failure.

To investigate this problem, a single-phase Cu–Sn alloy with good plasticity was selected to perform cold-spinning deformation experiments using a single spinning wheel [23]. Because the spinning part is a hollow cylinder, the wall thickness is small, and the plasticity is low. The use of a transmission electron microscope to characterize the sample increases the risk of further sample deformation during sample preparation. Alternatively, samples can

* Corresponding author.
** Corresponding author.
E-mail addresses: liuwg7@mail.sysu.edu.cn (W. Liu), wangbiao@mail.sysu.edu.cn (B. Wang).

https://doi.org/10.1016/j.jallcom.2020.154701
0925-8388/© 2020 Published by Elsevier B.V.

be characterized by mechanical derivation, simulation, and electron backscattering diffraction. Considering the changes in the microstructure and mechanical properties along the TD compared to those of the original billet, a comprehensive understanding of the local regional variation in cold deformation is crucial. According to the Keeg relation [24], the ultimate deformation rate of cold deformation is equal to the section shrinkage (~35%) of the material. However, one study [25] reported that the strength of a Cu–Sn alloy increased by 70%, whereas its plasticity remained in the range of 15%–20% after cold spinning. Unfortunately, after spinning, Cu–Sn alloys have low softening resistance and are in a substable state. This may be attributable to the considerable microstructural differences along the TD, which are the focus of the current study and represent a problem that must be solved in the future.

2. Material and methods

An annealed Cu–Sn alloy was selected as the test material. Table 1 shows its chemical composition, and Fig. 1 shows the grain structure of the billet. The grain size was approximately 9 μm, the ultimate tensile strength was 430 MPa, and the elongation was approximately 65%. Considering the spinning behaviour of Cu–Sn alloys, the main parameters of the spinning process were set as follows. The thinning rate was approximately 35%, and the feed ratio was approximately 0.7 mm/r. The spinning wheel moved along the feed direction, mainly by rotary wheel extrusion, to change the wall thickness; this further affected the material strength (Fig. 2). Samples were taken along the outer surface (0–1 mm), at an interior position (1–2 mm), and along the inner surface (2–3 mm) of the spinning part; these samples, and the original billet, were characterised by scanning electron microscopy and EBSD. To analyse the changes in the mechanical properties along the TD, tensile specimens with a thickness of 1 mm were selected on the outer surface, at the interior position, and on the inner surface of the spinning part and stretched at room temperature.

Finite element modelling of the spinning process was performed using a modelling method described elsewhere [12,13,17,20,24,26]. A mesh with a unit length of 1 mm was applied to the spinning parts. The type of friction affecting the spinning parts was shear friction, and the friction coefficient was set to 0.2. The type of contact between the spinning parts and the roller was automatic contact. Notably, the stress–strain variation along the TD during spinning was studied using the stress–strain model. The analysis results indicated that the stress–strain affected mainly the changes in microstructure along the TD.

3. Results and discussion

3.1. Mechanics analysis

Force analysis of the spinning wheel and the contact surface (Fig. 2) revealed that the contact surface was under triaxial stress during spinning. The radial compression (F_r), elongation deformation of the billet along the axial stress direction (F_z), and tangential stress (F_t) were small. After spinning, the billet extended mainly along the axial direction. In addition, because the total strain of the tangential deformation was very small, the triaxial deformation unit body can be simplified to a plane deformation model [21,22,24]. In the spinning deformation region, an element body with a width of *dz* (Fig. 3) was selected for stress analysis, and the differential equation of spinning deformation was established.

The equilibrium equations of the axial and radial forces on the unit body during spinning are as follows:

Table 1
Elemental distribution in the Cu–Sn alloy (wt%).

Sn	Al	Zn	Ni	Fe	Pb	P	Cu
9.7	0.002	0.1	0.087	0.01	0.01	0.17	Bal

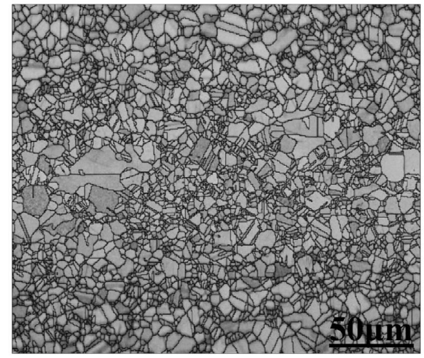

Fig. 1. Grain microstructure of the original Cu–Sn alloy sample.

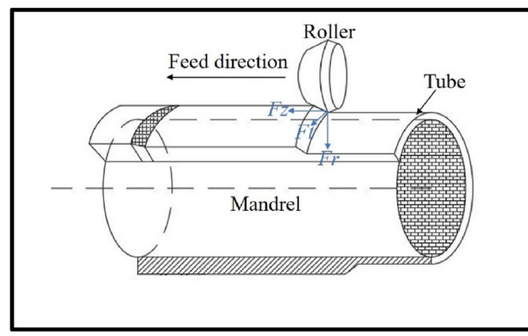

Fig. 2. Force analysis and simple diagram of spinning mode [13].

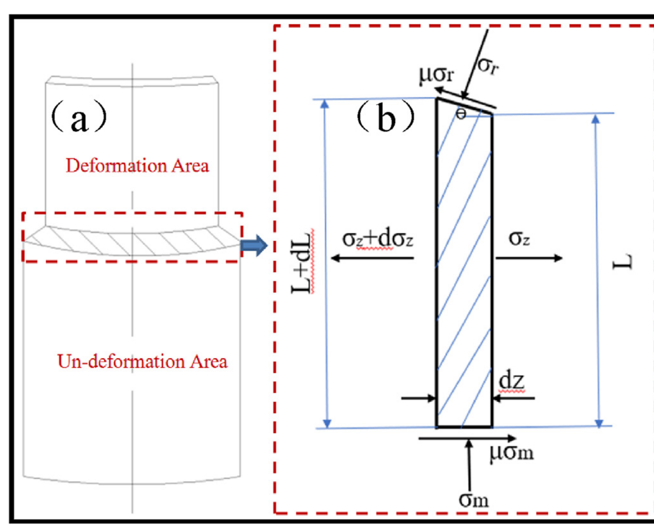

Fig. 3. Unit body in the deformation area was selected for force analysis neglecting tangential deformation, and the mechanical analysis of the plane model was conducted. (a) The shadow part represents the contact area between the roller and the tube. The deformation and the undeformed areas are defined as the area that the roller has passed through and the one that the roller has not passed, respectively. (b) The mechanical analysis of the contact area between roller and tube.

$$(\sigma_z + d\sigma_z)(L + d_L) + \sigma_r \frac{dz}{cos\theta} \sin\theta + \mu\sigma_r \frac{dz}{cos\theta} cos\theta - \sigma_z L - \mu\sigma_m d_z = 0 \tag{1}$$

$$\sigma_r \frac{dz}{cos\theta} cos\theta - \mu\sigma_r \frac{dz}{cos\theta} \sin\theta - \sigma_m d_z = 0 \tag{2}$$

where L is the height of the unit volume, σ_r is the radial stress, σ_z is the axial stress, σ_m is the force of the mandrel on dz, and μ is the friction coefficient. Combining (1) and (2) and using $dL = dz \tan\theta$ gives

$$Ld\sigma_z + \sigma_Z dL + \delta\sigma_m dL = 0 \tag{3}$$

In Eq. (3), $\delta = \frac{1+\mu^2}{1-\mu tan\theta}$. Under plane deformation, the plastic conditions satisfied by the stress are as follows:

$$\sigma_z + \sigma_m = 2\Big/\sqrt{3}\sigma_s \tag{4}$$

where σ_s is the yield point of the alloy. By substituting Eq. (4) into Eq. (3), the differential equation for spinning deformation is obtained:

$$\frac{d\sigma z}{(\delta - 1)\sigma z - \delta\sigma_\tau} = \frac{dL}{L} \tag{5}$$

In Eq. (5), $\sigma_\tau = \sigma_z + \sigma_m$. Integrating Eq. (5) and removing the logarithm gives

$$\sigma_z = \frac{\delta}{\delta - 1}\left(\sigma_\tau + \frac{t^{\delta - 1}}{\delta} C\right) \tag{6}$$

where C is an integral constant that depends on the boundary conditions, $L = L_0$, and $\sigma_{z0} = 0$. C is given by

$$C = \frac{\delta\sigma_\tau}{t_0^{\delta - 1}} \tag{7}$$

Substituting Eq. (7) into Eq. (6) gives

$$\frac{\sigma_z}{\sigma_\tau} = \frac{\delta}{\delta - 1}\left\{1 - \left(\frac{L}{L_0}\right)^{\delta - 1}\right\} \tag{8}$$

First, under normal spinning deformation, $\frac{\sigma_z}{\sigma_\tau}$ in Eq. (8) is less than 1; θ does not change during spinning. The thinning rate has the strongest effect on the stress distribution. The δ value is generally between 1.2 and 2 [24]. Next, the δ value ($1.2 \leq 1.5 \leq 2$) were substituted in Eq. (8), and the results were calculated, as shown in Fig. 4. It can be clearly found that as $\frac{L}{L_0}$ increases, $\frac{\sigma_z}{\sigma_\tau}$ decreases, and the curves for different δ values decreased monotonically. Because $\sigma\tau = \sigma z + \sigma m$, Eq. (8) can be written as

$$\frac{\sigma_z}{\sigma z + \sigma m} = \frac{\delta}{\delta - 1}\left\{1 - \left(\frac{L}{L_0}\right)^{\delta - 1}\right\} \tag{9}$$

As the thickness L increases, the value of the right-hand side of Eq. (9) decreases gradually. The right-hand side of the equation divided by σ_m/σ_z was found to be proportional to L. That is, a larger thickness corresponded to a greater σ_m/σ_z ratio and vice versa. However, the sensitivity to σ_m was much greater than that to σ_z. Therefore, σ_m, σ_z, and σ_r were all found to change the TD structure during spinning; that is, these changes were not the effect of the radial force alone. Mechanical analysis revealed that the forces acting on the spinning parts represented the combined action of three-dimensional forces. As the thickness of the spinning parts gradually decreases, the difference in the local force acting on the spinning parts may lead to a gradual decrease in plastic deformation from the outer surface to the inner surface.

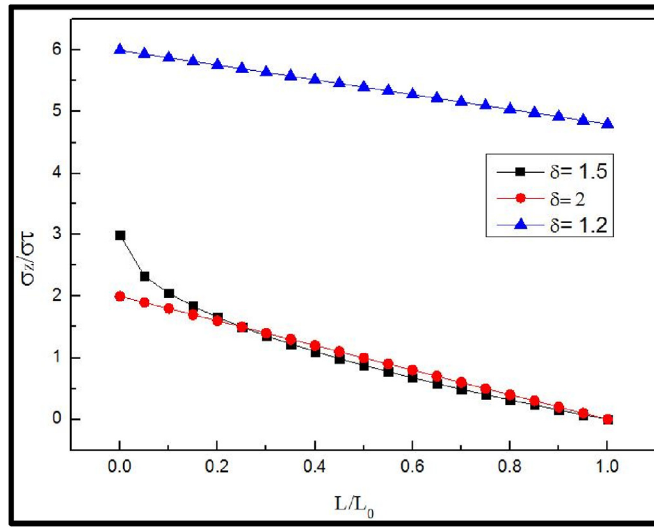

Fig. 4. The curve shows the relationship between $\frac{\sigma_z}{\sigma_\tau}$ and $\frac{L}{L_0}$ under different δ (1.2, 1.5, and 2.).

3.2. Microstructure during spinning

After spinning, samples were taken from the outer surface, the inner surface, and the middle of the spinning part. The grain size and grain orientation were analyzed by EBSD, and the results are shown in Fig. 5. In Fig. 5(a_1)–5(c_1), each colour represents a grain orientation; the grain orientation diagram indicates that the grain orientation varied randomly. Furthermore, the inverse pole graphs in Fig. 5(a_2)–5(c_2) indicate that the density of the texture pole was low and the texture arrangement was scattered. Thus, the grains exhibited no preferred orientations. In Fig. 5(a_3)–5(c_3), the grain sizes of the outer surface, the middle part and the inner surface are analyzed, respectively.

Based on the finite element analysis, the spinning process of Cu Sn alloy was simulated, The stress and strain changes during spinning were simulated. Fig. 6(a) presents a cross-sectional view of the stress distribution of the spinning piece. Area I represent the spinning failure region, area III indicates the base of the screwdriver without spinning, and area II is the effective observation region. Fig. 6(b) shows the stress variation during spinning. The stress along the TD was observed to decrease gradually. The stress increased gradually along the spinning direction as a result of metal accumulation. Similarly, Fig. 6(c) presents a cross-sectional view of the strain distribution of the spinning piece; the strain decreases gradually along the TD. In particular, the inner surface strain was less than 1%(Fig. 6(d)); this observation also explains why the inner surface grains retained many of the original GBs.

Fig. 7 displays the GB misorientation of the original sample and the spinning piece in the TD; the green and black lines represent low-angle grain boundaries (LAGBs) and high-angle grain boundaries (HAGBs), respectively. As shown in Fig. 7(a), most of the GBs were HAGBs. The peak misorientation value appeared at 60°. After spinning, as shown in Fig. 7(b), the peak GB misorientation on the outer surface of the spun piece shifted leftward, and the peak appeared at 0°–5°. Most of the LAGBs were distributed in the coarse grain region, which is particularly evident in Fig. 7(b)–(c).

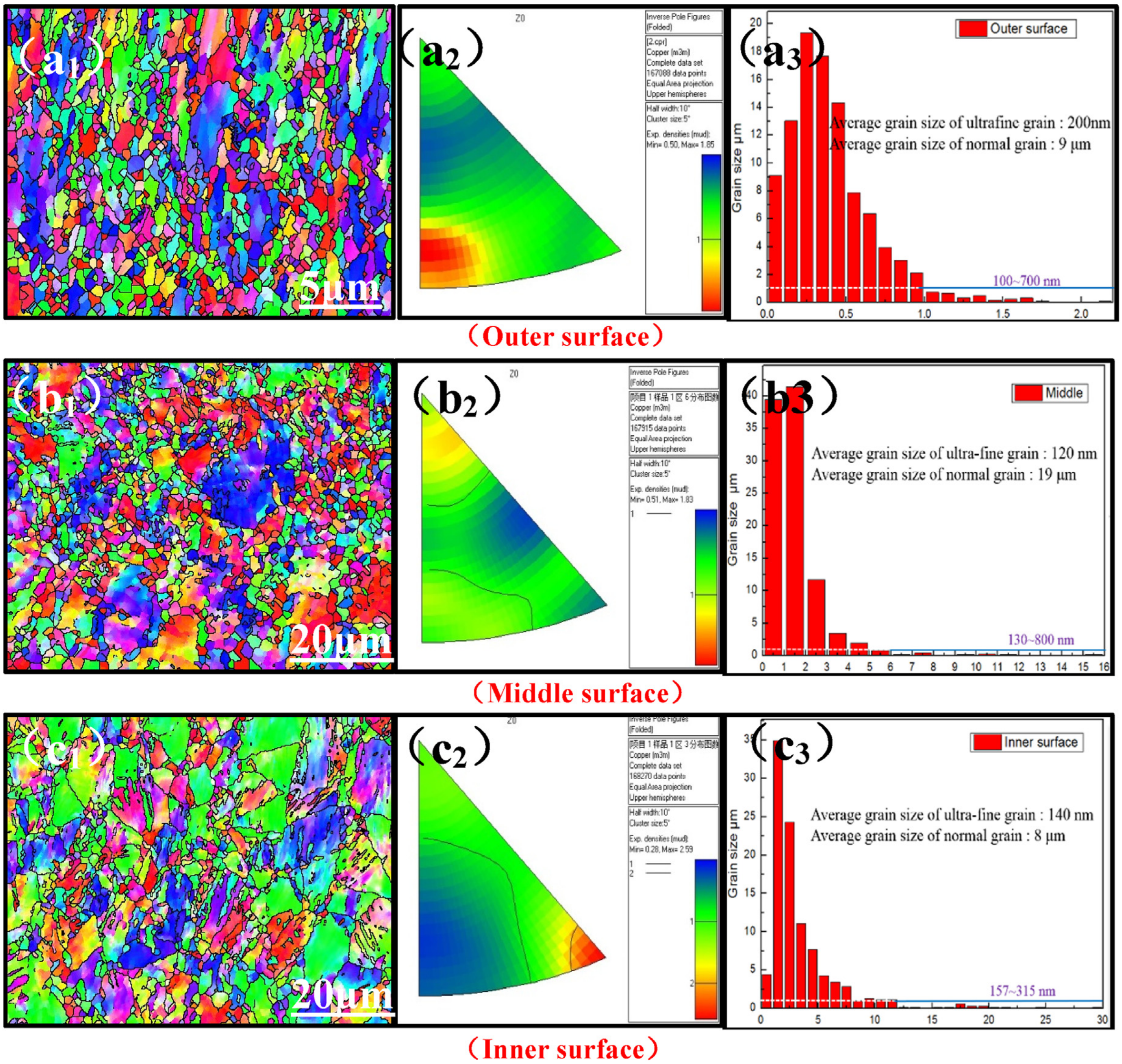

Fig. 5. After spinning, EBSD experiments were carried out on the outer surface, middle part and inner surface, respectively. (a_1), (b_1), and (c_1) show the grain orientations, and each colour represents a different grain orientation. (a_2), (b_2), and (c_2) are the Polar graphs. (a_3), (b_3), and (c_3) show the grain size distributions. (For interpretation of the references to colour in this figure legend, the reader is referred to the Web version of this article.)

This phenomenon is associated mainly with the GB angle of ultrafine grains. The deformation behaviour of ultrafine grains is controlled by dislocation. Dislocation source activation is suppressed in superfine grains, making it difficult for a subgrain boundary to form. In addition, dislocation sources are often no longer present in the grain interior of ultrafine-grained materials [26–31]. Notably, an ultrafine GB is a high-energy GB [32,33], and the annihilation probability of dislocation is much greater in a high-energy GB than in a low-energy LAGB. Most of the LAGBs were distributed in large deformed grains. Because of the effect of strain hardening, the dislocations accumulate in the deformed coarse grain, and it is easy for the dislocations to move outward and form a subgrain boundary. The grain size increased gradually from the outer surface to the inner surface, and the ultrafine grains were gradually replaced by common coarse grains, indicating that the LAGB increased, and the distribution of the subgrain boundary became denser.

Fig. 7 shows that the GB energy (GBE) changed as the misorientation migrated. To explain this phenomenon, we attempted to construct the energy relationship of the GB and model the GBE at different GB angles. The LAGB had a dislocation network structure, and its energy was approximately equal to the dislocation energy; therefore, the dislocation energy of a unit length on the GB can be expressed as follows [34]:

$$E_d = \frac{G\boldsymbol{b}^2}{4\pi(1 - \nu)} ln\frac{D}{r_0} + E_0 \tag{10}$$

where G is the shear modulus, E_0 is the core energy of the dislocation, D is the dislocation spacing, r_0 is the radius of the dislocation of the elastic stress field ($r_0 \approx b$), and $\boldsymbol{b}$ is the Burgers vector. The number of dislocations per unit area is the GB misorientation, $\theta/\boldsymbol{b}$. Therefore, the GBE per unit area can be obtained [35].

$$E_{LAGB} = \frac{\theta}{\boldsymbol{b}}E_d = \frac{E_d}{D} = \frac{Gb\theta}{4\pi(1 - \nu)} ln\frac{1}{\theta} + \frac{\theta}{\boldsymbol{b}}E_0 \tag{11}$$

The GBE per unit length, E_{LAGB}, was obtained according to the dislocation of the stress field [34,35].

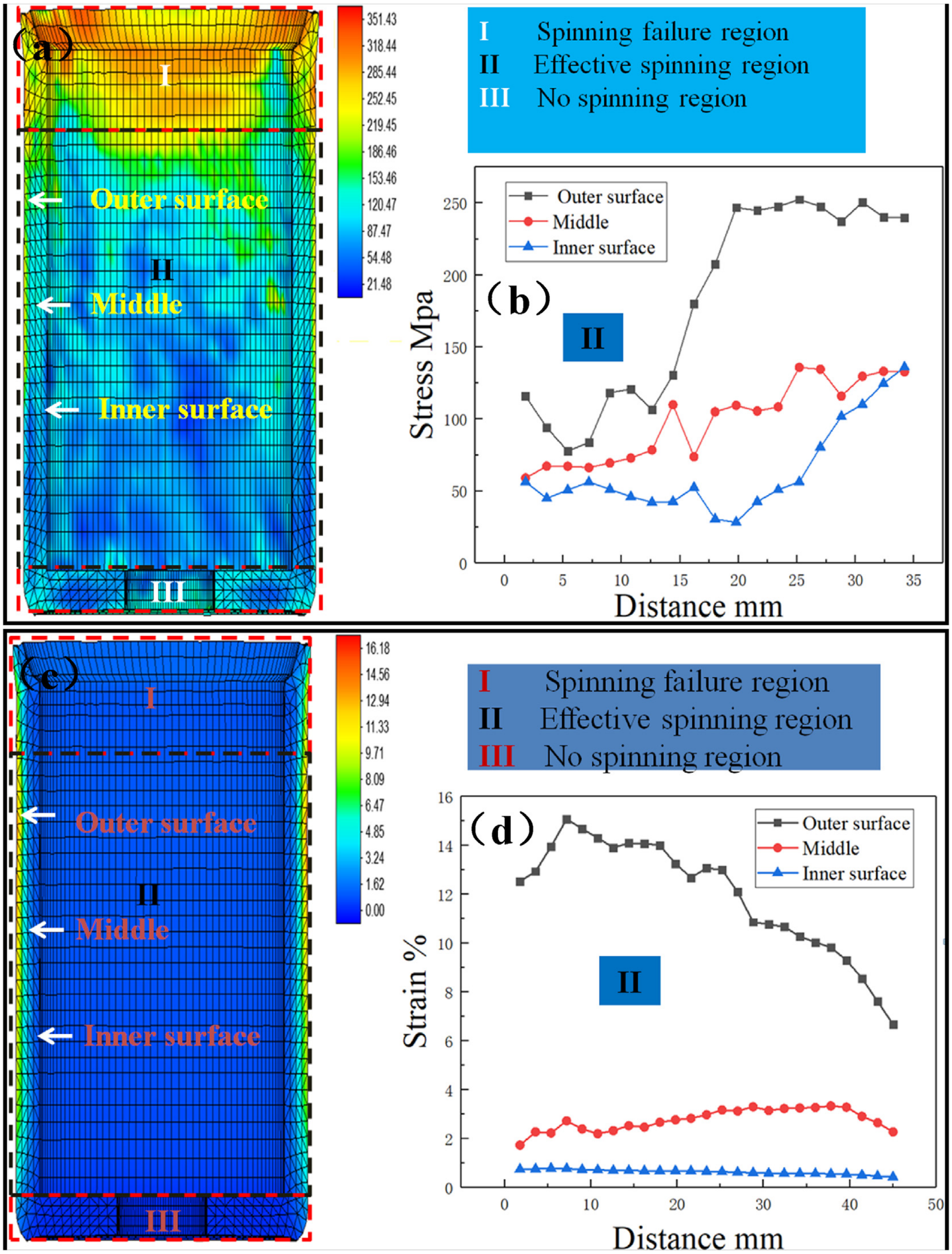

Fig. 6. The effective positions of spinning parts as obtained by finite element simulation and the calculated stress–strain variation along the TD. (a) Stress distribution of spinning parts along TD after spinning simulation, (b) the calculated numerical distribution of stress on different surfaces, (c) strain distribution of spinning parts along TD after spinning simulation, and (d) the calculated numerical distribution of strain on different surfaces.

$$E_{LAGB} \approx \frac{Gb^2}{4\pi(1-\nu)} ln \frac{eD}{2\mu\pi b} \quad (12)$$

where e is a constant, $\mu = \frac{r_0}{b}$, and $D = \boldsymbol{b}/\theta$. We can rewrite Eq. (12) as

$$E_{LAGB} = \frac{Gb^2\theta}{4\pi(1-\nu)} ln \frac{eD}{8\pi\theta} = E\theta(\phi - ln\theta) \quad (13)$$

In Eq. (13), $E = \frac{Gb}{4\pi(1-\nu)}$, and $\phi = 1 - \ln\left(\frac{2\pi r_0}{\boldsymbol{b}}\right)$.

In Eq. (13), E_{LAGB} initially increases with increasing θ. The calculated GB misorientation is displayed in Fig. 8. By evaluating the behaviour of the two curves, we discovered that the frequency of LAGBs increased gradually along the TD. Notably, LAGBs were much more common than HAGBs; therefore, it can be concluded that an approximate gradient change in the GBE occurred along the TD, and it decreased gradually along the TD.

It was impossible to construct HAGBs with dislocations [35]. Eq. (13) shows that the energy of LAGBs is mainly an elastic property of the dislocation stress field, whereas the energy of HAGBs is mainly

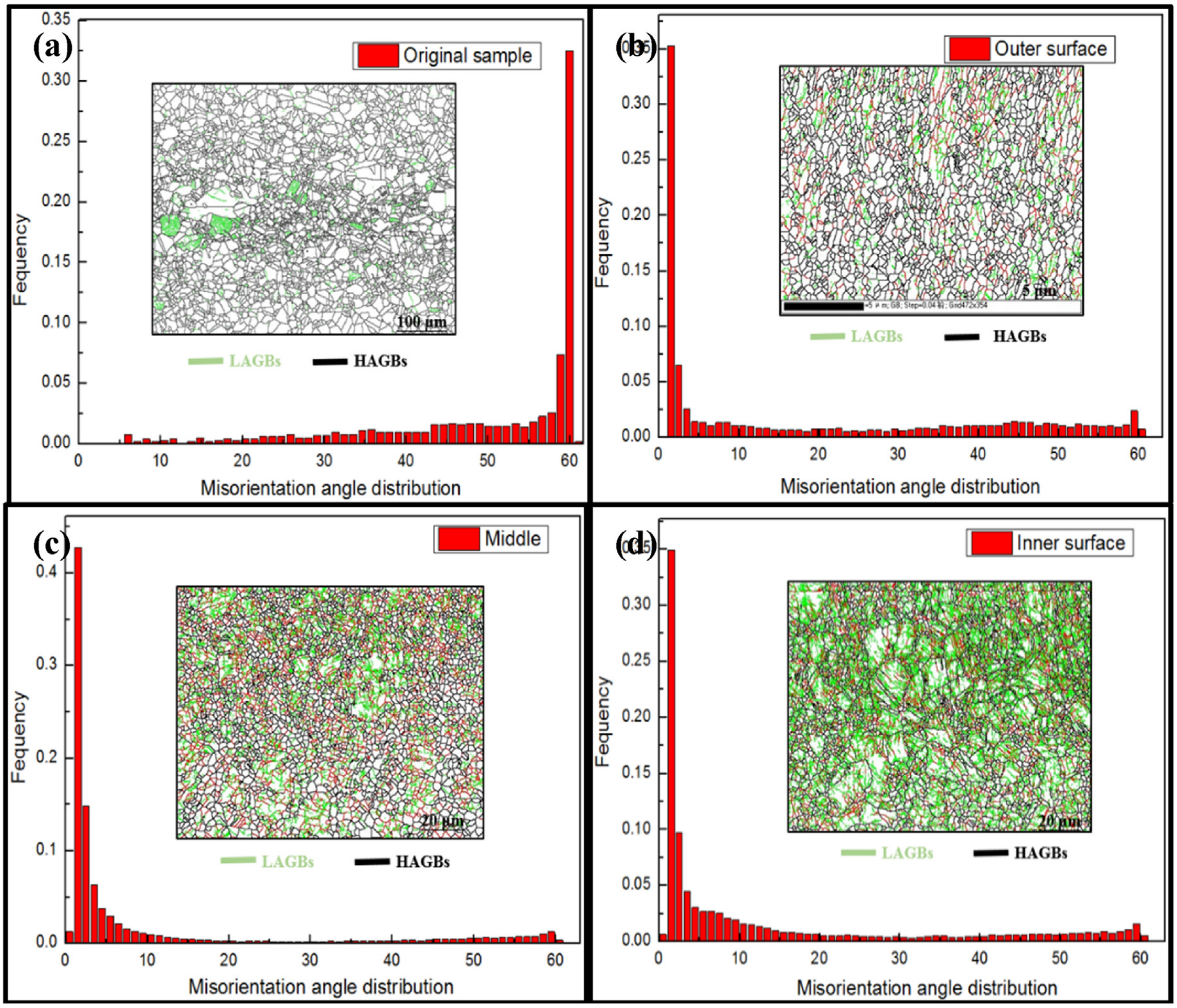

Fig. 7. The distribution characteristics of the grain boundary angle on the different surfaces of the spinning parts were measured by EBSD. Histogram indicates the changes in grain misorientation. In the misorientation diagram, the green and black curves represent the LAGBs and ordinary grain boundaries, respectively. (For interpretation of the references to colour in this figure legend, the reader is referred to the Web version of this article.)

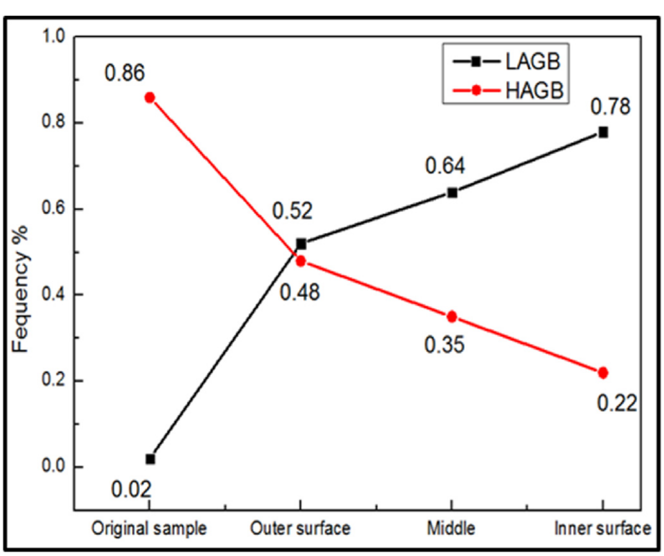

Fig. 8. Distribution of proportions of the LAGBs and HAGBs along the TD.

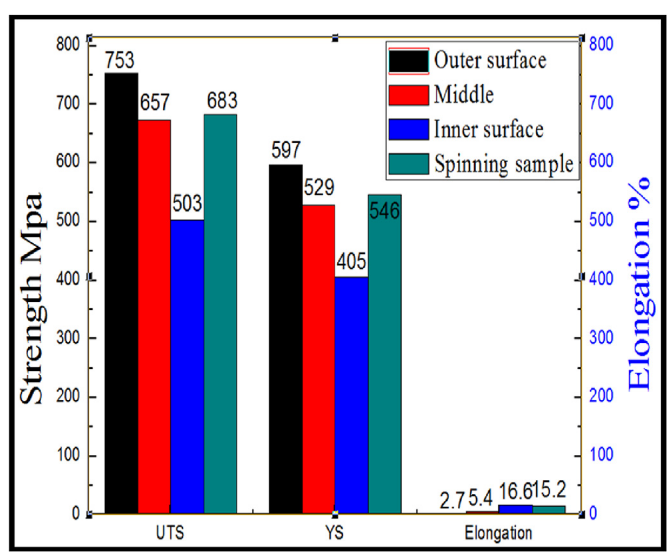

Fig. 9. Ultimate tensile strength (UTS), yield strength (YT) and the elongation of Cu–Sn alloys at different sampling positions.

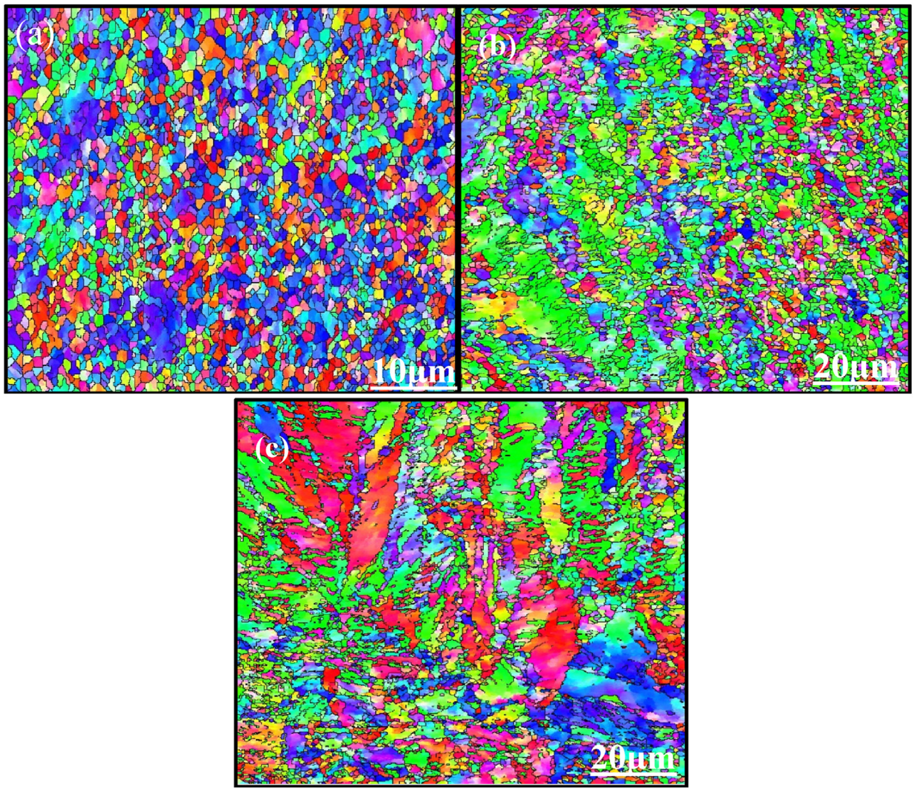

Fig. 10. Grain distribution characteristics of tensile specimens: (a) outer surface, (b) middle, and (c) inner surface.

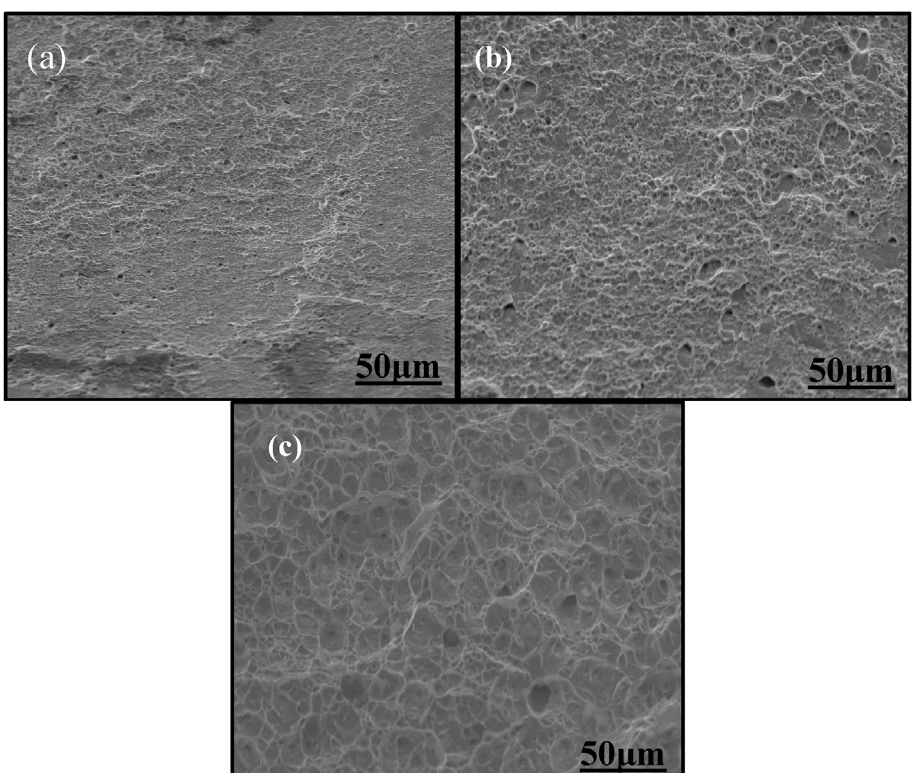

Fig. 11. Tensile fracture characteristics of Cu–Sn alloy spinning parts: (a) outer surface, (b) middle, and (c) inner surface.

the core energy of the dislocation stress field [35,36], which has remained a challenge in related research [36–39]. According to an empirical formula, the total strain energy of dislocations can be expressed as follows [31]:

$$E = \alpha \mathrm{Gb}\theta + E_{LAGB} + E_{HAGB} \quad (14)$$

where α is a constant. Therefore, the GBE of the HAGBs can be obtained [30]:

$$E_{HAGB} = \alpha \mathrm{Gb}\theta - E\theta(\phi - ln\theta) \quad (15)$$

In Fig. 8, the distribution frequency of grain boundary angles is quantitatively analyzed. It can be found that the distribution frequency of LAGBs increases and that of HAGBs decreases. According to the results of Eq. (15), the GBE of the HAGBs decreases with increasing number of LAGBs, and the proportion of HAGBs also decreases gradually. With regard to the microstructural changes, because cold deformation was applied, the probability of LAGBs merging and growing to form a HAGB was very low [37,38]. That is, the increase in the GBE along the TD represented mainly the increase in LAGBs, and the proportion of LAGBs was inversely proportional to that of HAGBs. This result suggests that the GBE is a function of the misorientation.

3.3. Mechanical properties and microstructural analysis after tensile testing

3.3.1. Mechanical properties analysis

To further understand the tensile properties of the outer, middle and inner surfaces of Cu–Sn alloy spinning parts, the mechanical properties of different samples of the Cu–Sn alloys were tested and shown in Fig. 9, the mechanical properties of different samples of the Cu–Sn alloys were tested. Because ultrafine grains were present and the grain size was smallest, the GBE was highest on the outer surface, indicating maximum strength and minimal plasticity on that surface. Along the TD, the ultimate tensile strength decreased from 753 to 503 MPa, and the elongation increased from 2.7% to 16.6%. Interestingly, the strength of the spinning part of the outer surface sample was comparable to that of the interior sample, and the plasticity of the interior sample was only lower than that of the inner surface sample. The spinning part combined the characteristics of the outer surface, interior, and inner surface samples; therefore, the spinning part had high strength and high elongation. However, the inner surface had low strength, and the outer surface had low plasticity.

3.3.2. Microstructural analysis

After the samples were stretched, the EBSD was observed at a distance of approximately 1 mm from the tensile fracture; the grain distribution characteristics are displayed in Fig. 10. Fig. 10(a) shows that the grains on the outer surface exhibited little elongation, which also explains the low plasticity of the outer surface. As indicated in Fig. 10(b) and (c), the grains were elongated along a certain direction. Specifically, the coarse grains on the inner surface were elongated and demonstrated greater plasticity during stretching. This variation in the plasticity is reflected in the fracture characteristics. As presented in Fig. 11, the number of dimples increased gradually along the TD; this also reflects the trend of increasing plasticity along the TD.

4. Conclusion

(1) The gradient distribution of the spinning deformation was resulted from the gradual decrease in plastic deformation from the outer layer to the inner layer caused by the local spinning deformation load. Under strain hardening, the ultrafine grains on the outer surface also affected the distribution of the work-hardening structures, such as the subgrain boundaries. The strengthening of the outer surface was induced by strain hardening and ultrafine grain strengthening, and the GBE decreased gradually along the TD.

(2) The strength improvement was attributed mainly to the high strength near the outer surface of the spinning parts. The high plasticity of the spinning parts resulted mainly from the high plasticity of the inner surface. The coordination of the TD ensured high strength and plasticity in the spinning parts. Furthermore, the outer surface had the highest strength.

Declaration of competing interest

There is no conflict of interest between authors.

CRediT authorship contribution statement

Jun Hui: Formal analysis, Writing - original draft. **Wenguan Liu:** Funding acquisition, Writing - review & editing. **Biao Wang:** Funding acquisition, Writing - review & editing.

Acknowledgements

The work was supported by the National Natural Science Foundation of China through the funds 11832019, 51601212, 11472313, 11572355.

References

[1] A.El Hassanin, A. Astarita, On the manufacturing of a gas turbine engine Part Through metal spinning process, in: AIP Conference Proceedings, 2018, https://doi.org/10.29007/sbcv.

[2] O. Music, J.M. Allwood, K. Kawai, A review of the mechanics of metal spinning, J. Mater. Process. Technol. 210 (2010) 3–23.

[3] M. Sivanandini, S.S. Dhami, B.S. Pabla, Flow forming of tubes-a review, Int. J. Sci. Eng. Res. 3 (2012) 1–11.

[4] M.L. Alves, B.P.P. Almeida, P.A.R. Rosa, P.A.F. Martins, End forming of thin-walled tubes, J. Mater. Process. Technol. 177 (2006) 183–187.

[5] P.A.R. Rosa, J.M.C. Rodrigues, External inversion of thin-walled tubes using a die: experimental and theoretical investigation, Int. J. Mach. Tool Manufact. 43 (2003) 787–796.

[6] H.R. Molladavoudi, F. Djavanroodi, Experimental study of thickness reduction effects on mechanical properties and spinning accuracy of aluminium 7075-O, during flow forming, Int. J. Adv. Manuf. Technol. 52 (2011) 949–957.

[7] A.R. Fazeli, M. Ghoreishi, Investigation of effective parameters on surface roughness in thermomechanical tube spinning process, Int. J. Material Form. 2 (2009) 261–270.

[8] B. Rentsch, N. Manopulo, P.N. Hora, Umerical modelling, validation and analysis of multi-pass sheet metal spinning processes, Int. J. Material Form. 10 (4) (2017) 641–651.

[9] A.P. ghasafari, M. Salimi, A. Daraei, Flow stress evaluation in hot rolling of steel, J. Mater. Eng. Perform. 23 (2014) 2819–2828.

[10] W.C. Xu, D.B. Shan, Hot spinning process of cylindrical workpieces of TA15 titanium alloy, Rare Met. 26 (2007) 255–261.

[11] W.C. Xu, D.B. Shan, Effect of spinning deformation on microstructure evolution and mechanical property of TA15 titanium alloy, T. Nonferr. Metal. Soc 17 (2007) 1025–1211.

[12] W.C. Xu, X.K. Zhao, Numerial simulation and experimental study on multi-pass stagger spinning of internally toothed gear using plate blank, J. Mater. Process. Technol. 229 (2016) 450–466.

[13] W.C. Xu, X.K. Zhao, Influence of roller distribution modes on spinning force during tube spinning, Int. J. Mech. Sci. 113 (2016) 10–25.

[14] W.C. Xu, X.K. Zhao, Fabrication of curved generatrix workpiece of TA15 titanium alloy by variable thickness tube spinning and flaring process, Int. J. Adv. Manuf. Technol. 88 (2017) 1983–1992.

[15] A.R.K. Hazawi, R.K. Abdel-Magied, M.N. Elsheikh, An experimental analysis of a flaring process for tube ends using a novel spinning tool, Int. J. Adv. Manuf. Technol. 34 (2017) 157–165.

[16] A.R. Fazeli, M. Ghoreishi, Statistical analysis of dimensional changes in

thermomechanical tube-spinning process, Int. J. Adv. Manuf. Technol. 52 (2011) 597–607.
[17] K. Essa, P. Hartley, Numerical simulation of single and dual pass conventional spinning processes, Int. J. Material Form. 2 (2009) 271–281.
[18] M. Murata, T. Kuboki, T. Murai, Compression spinning of circular magnesium tube using heated roller tool, J. Mater. Process. Technol. 162–163 (2005) 540–545.
[19] M.A. Rasoli, A. Abdullah, M. Farzin, T.A. Fadaei, Influence of ultrasonic vibrations on tube spinning process, J. Mater. Process. Technol. 212 (2012) 1443–1452.
[20] X.K. Zhao, W.C. Xu, Influence of roller distribution modes on spinning force during tube spinning, Int. J. Mech. Sci. 113 (2016) 10–25.
[21] M. Zhan, H. Yang, Review on hot spinning for difficult-to-deform lightweight metals, T. Nonferr. Metal. Soc 25 (2015) 1732–1743.
[22] M. Zhan, H.D. Zhai, Springback mechanism and compensation of cryogenic Ti alloy tube after numerically controlled bending, T. Nonferr. Metal. Soc. 22 (2012) 287–293.
[23] J. Hui, Z.X. Feng, The influence of power spinning and annealing temperature on microstructures and properties of Cu-Sn alloy, Mater. Char. 144 (2018) 611–620.
[24] S.X. Chen, Strong Spinning Process and Equipment, National Defense Industry Press, 1986.
[25] J. Hui, Z.X. Feng, Microstructural evolution analysis of grains and tensile properties of tin bronze in hot extrusion at different temperatures, Mater. At. High. Temp 36 (2018) 68–75.
[26] H. Zoghi, A.F. Arezoodar, M. Sayeaftabi, Enhanced finite element analysis of material deformation and strain distribution in spinning of 42CrMo steel tubes at elevated temperature, Mater. Des. 47 (2013) 234–242.
[27] Z. Pater, J. Tomczak, Experimental and numerical analysis of helical-wedge rolling process for producing steel balls, Int. J. Mach. Tool Manufact. 67 (2013) 1–7.
[28] D. Qian, Y. Pan, 3D coupled macro–microscopic finite element modelling and simulation for combined blank-forging and rolling process of alloy steel large ring, Comput. Mater. Sci. 70 (2013) 24–36.
[29] Y.T. Zhu, X.L. Wu, Dislocation–twin interactions in nanocrystalline fcc metals, Acta Mater. 59 (2011) 812–821.
[30] K.S. Kumar, V. Swygenhoven, Mechanical behavior of nanocrystalline metals and alloys, Acta Mater. 51 (2003) 5743–5774.
[31] Y.T. Zhu, X.Z. Liao, Deformation twinning in nanocrystalline materials, Prog. Mater. Sci. 57 (2012) 1–62.
[32] L. Lu, Y.F. Shen, K. Lu, Ultrahigh strength and high electrical conductivity in copper, Science 304 (2004) 422–426.
[33] X.C. Liu, H.W. Zhang, K. Lu, Strain-induced ultrahard and ultrastable nanolaminated structure in nickel, Science 342 (2013) 337–340.
[34] M.A. Meyers, A. Mishra, Mechanical properties of nanocrystalline materials, Prog. Mater. Sci. 51 (2006) 427–556.
[35] I. Kovacs, L. Zsoldos, Dislocation and Plastic Deformation, Pergamon, Oxford (UK), 1973.
[36] X.Z. Liao, S.G. Srinivasan, Formation mechanism of wide stacking faults in nanocrystalline Al, Appl. Phys. Lett. 84 (2004) 3564–3566.
[37] H. Wu, W.C. Xu, Mechanism of increasing spinnability by multi-pass spinning forming - analysis of damage evolution using a modified GTN model, Int. J. Mech. Sci. 159 (2019) 1–19.
[38] M. Ichimuraa, J. Narayan, Atomistic study of dislocation nucleation in Ge/(001) Si heterostructuses, Philos. Mag. A 72 (1995) 281–295.